Hindawi
International Journal of Photoenergy
Volume 2022, Article ID 4697980, 17 pages
https://doi.org/10.1155/2022/4697980

Research Article

Structural Optimization and Thermal Management with PCM-Honeycomb Combination for Photovoltaic-Battery Integrated System

Xinxi Li,[1] **Jiangyun Zhang**,[1] **Dequan Zhou**,[1] **Guoqing Zhang**,[1] **Hongwei Wu**,[2] **and Rensheng Liu**[3]

[1]*School of Materials and Energy, Guangdong University of Technology, Guangzhou, Guangdong 510006, China*
[2]*School of Physics, Engineering and Computer Science, University of Hertfordshire, Hatfield AL10 9AB, UK*
[3]*ShunDe SYSU Institute for Solar Energy, Foshan, Guangdong 528311, China*

Correspondence should be addressed to Jiangyun Zhang; roseyyun@163.com

Received 10 November 2021; Accepted 30 April 2022; Published 25 May 2022

Academic Editor: Gianluca Coccia

Power lithium–ion batteries retired from the electric vehicles (EVs) are confronting many problems such as environment pollution and energy dissipation. Traditional photovoltaic (PV) battery systems are exhibiting many issues such as being bulky and expensive, high working temperature, and short service span. In order to address these problems, in this study, a novel PV–battery device integrating PV controllers and battery module into an independent device is proposed. Phase change material (PCM) as the energy storage material has been utilized in battery module, and the aluminum honeycomb is combined with PCM to improve the heat conductivity under natural convection conditions. Three types of PV battery systems including the general PV–battery integrated system (G–PBIS), honeycomb PV–battery integrated system (H–PBIS), and honeycomb–paraffin PV–battery integrated system (HP–PBIS) have been investigated in detail. The results reveal that the maximum temperature of the HP–PBIS coupling with the double–layer $10 \times 165 \times 75\,mm^3$ PCM was reduced to 53.72°C, exhibiting an optimum cooling effect among various PV battery systems. Thus, it can be concluded that the aluminum honeycomb provides the structural reliability and good thermal conductivity, and the PCM surrounding battery module can control the temperature rising and balance the temperature uniformly. Besides, the optimum PV–battery integrated system performs a promising future in energy storage fields.

1. Introduction

With the global shortage of fossil fuels and the aggravation of environmental pollution, countries are vigorously promoting the use of renewable energy and improving the energy efficiency such as solar energy and wind power [1, 2]. The photovoltaic (PV) power generation has been regarded as an inventible source of green energy owing to its natural advantages such as low operational cost, low maintenance, high availability, and reliability. However, the use of solar energy depends on weather conditions to a large extent, which are intermittent and unstable. Hence, a power storage device such as a battery is required to store excessive power during off-peak hours and supplied to power electrical equipment during peak hours to ensure that a reliable power source [3, 4]. Many challenges have been encountered in traditional PV energy storage applications and their manufacturing processes, such as connecting PV systems with battery modules, installation locations, high installation cost, maintenance

cost, and structural reliability issues. The aforementioned problems are urgently needed to solve for speeding up the PV system development [5, 6].

In recent years, some investigations have focused on integrating photovoltaics with batteries into a system. To provide a scalable and compact power supporting solution to the system, there are many endeavors that have been carried out for designing and exploring corresponding portable electronic devices. Ravi et al. [7] conducted an optimized solar PV/battery energy storage off-grid integrated renewable energy system. The proposed energy system exhibited a remarkable energy-saving effect. Li et al. [8] proposed a small hybrid power system of PV cell and sodium borohydride hydrolysis-based fuel cell. The experimental results indicated that the aforementioned system could switch the power supply automatically and timely under various emergency conditions, and the output voltage remains stable all the time. Fang et al. [9] developed a two-layer game theoretic microgrid capacity optimization scheme considering uncertainty of renewable energy. The corresponding data confirmed the effectiveness of the proposed model. Solomon et al. [10] utilized triple-junction thin-film silicon solar cell connecting directly to a lithium ion battery to realize the charging of the battery and in turn discharging the battery through the solar cell, which showed that an appropriate voltage matching the solar cell provided efficient charging for lab-format lithiumion storage battery, and this simple integrated device performed good sustainability. Grzesiak et al. [11] put forward a portable PV module that was combined with the battery and innovative system for power management. It was an innovative system that quickly and accurately supporting the elevation and declination angle and monitoring the state of charge (SOC) and discharge of the module. Besides, Vega-Garita et al. [12] proposed a device combining all the components of a solar-battery system in one device, and the results revealed that a thermal analysis using finite element method models and prototype experiments could confirm its feasibility. However, few studies have investigated the controlling-temperature performance of the battery in the PV-battery integrated equipment. Besides, the temperature of the silicon layer and the structural strength of the device are also rarely mentioned in the present research.

Phase change material (PCM) has been widely utilized in heat storage owing to the capability of releasing and storing large amount of latent heat during melting and solidification process [13, 14]. Bouadila et al. [15] presented new solar air collectors with a packed-bed latent heat storage system using PCM spherical capsules. Kabeel et al. [16] investigated the parameters that could affect the thermal performance of the flat and v-corrugated plate solar heat collectors with/without using built-in PCM as thermal energy storage material. Khadraoui et al. [17] studied solar collectors with/without PCM, which is aimed at evaluating the thermal performance of PCM unit, and the results revealed that PCM in solar collectors could increase the outlet air temperature of the collector. Besides, it had desirable temperature range for battery thermal management, which could also be applied in PV-battery integrated equipment.

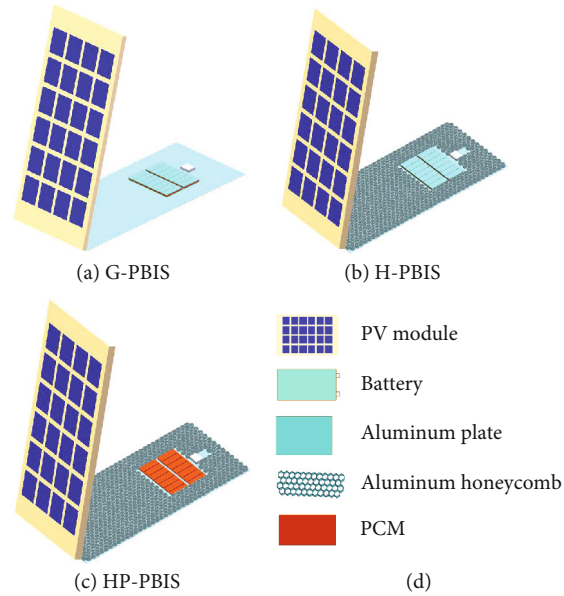

Figure 1: Geometric model designs of PBIS: (a) G–PBIS, (b) H–PBIS, (c) HP–PBIS and (d) Description of PBIS components.

Recently, honeycomb structure materials have attracted much attention in many fields. Honeycomb with lightweight loading structure can not only provide various sizes and thickness according to the device but also support with good mechanical and thermal performance. Besides, installing a honeycomb core between materials can obviously improve crash resistance and stable deformation performances [18, 19]. The honeycomb structure fin structure in a heat storage panel can be benefit for improving the thermal conductivity of PCM for increasing the thermal management effectiveness [20–22]. Abuska et al. [23] investigated the effect of honeycomb core on the latent heat storage with PCM in solar air heater. The experimental data showed that the daily efficiency was improved by 2.6–22.3 and charge-discharge times was significantly shortened owing to the participation of honeycomb. Hasse et al. [24] presented that honeycomb panels with PCM, which could improve the thermal conductivity and avoid the leakage phenomenon. Xie et al. [25] put forward a composite material combined the shape–stabilized PCM with aluminum honeycomb applied in thermal controlling, and the results demonstrated that the participation of aluminum honeycomb structure could maintain the temperature variation of the heating source within a much smaller range. Abuşka et al. [26] proposed a novel solar air collector consisting the PCM–Rubitherm RT54HC of aluminum honeycomb, furtherly focused on effect of using honeycomb core on the collector thermal performance regarding heat storage with PCM under natural convection condition. Nevertheless, the PCM–honeycomb structure has already been utilized; it should be further exploring a PV device with battery module to obtain much longer and more stability lifetime in practical application.

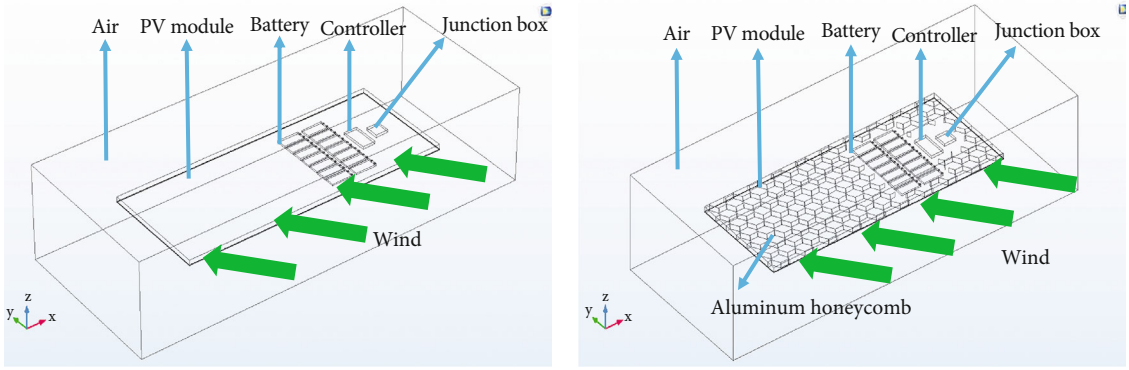

(a) (b)

Figure 2: The schematic of the PV–battery integrated systems: (a) G–PBIS, and (b) H–PBIS.

Power lithium–ion batteries retired from electric vehicles (EVs)/hybrid electric vehicles (HEVs) always bring about many severe issues, such as environment pollution and energy waste [27–30]. On the contrary, if the retired batteries could be utilized furtherly, they not only provide a circular economy possibility but also improve the efficiency of energy. PV–battery system is a promising research orientation because it can absorb the heat energy from solar and storage the energy in batteries. Until now, there are few researches on the thermal management of heat storage equipment including battery module with aluminum honeycomb and PCM. In this study, a novel PV–battery system integrating PV controllers and battery module into an independent device is proposed. Moreover, the aluminum honeycomb and PCM are combined for carrying out thermal management and the evaluation of heat dissipation performance. Hence, this study is aimed at investigating the thermal behaviors of the PV–battery integrated system.

2. Model and Solution

2.1. Designs for the Geometric Model. There were two basic geometric model designs of PV–battery integrated system (PBIS) with a PV module as outer shell in this study. As shown in Figure 1(a), it was the general PV–battery integrated system (G–PBIS) and the air domain with the size of $3000 \times 1200 \times 600\ mm^3$ (length × width × height). The PV module size was $3000 \times 1200 \times 600\ mm^3$ (length × width × height), which contained 2×7 battery arrays, a controller, and a junction box. The sizes of the single battery, the controller, and junction box were $160 \times 75 \times 10\ mm^3$ (length × width × height), $100 \times 200 \times 15\ mm^3$ (length × width × height), and $100 \times 100 \times 15\ mm^3$ (length × width × height), respectively. From Figure 1(b), it showed the honeycomb PV–battery integrated system (H–PBIS) and the air domain. It could be observed that the H–PBIS with several additional aluminum honeycombs surrounds the batteries as their array. Besides, the controller and the junction box are put inside of H–PBIS. Additionally, Figure 1(c) describes the structure of honeycomb–paraffin PV–battery integrated system (HP–PBIS).

Table 1: Physical property parameters used in the simulation.

Materials	ρ (kg·m^{-3})	c (J·kg^{-1}·k^{-1})	k (W·m^{-1}·k^{-1})	μ (Pa·s)
Aluminum	2719	871	202.4	—
Battery	2705	1756	2	—
EVA	960	2090	0.35	—
Glass	3000	500	1.8	—
Si	2330	677	148	—
Junction box	1760	1.463	0.1	—
Converter	1100	1300	0.3	—
Air	1.169	1.004	0.02	17.9×10^{-6}
PCM	1355	1975	1.5	—

It is worth noting that the differences between G–PBIS and H–PBIS were that several additional aluminum honeycombs filled with space other than the battery array, the controller, and the junction box in H–PBIS, as shown in Figure 2. Moreover, the flow of wind during natural cooling is described in Figure 2. The size of aluminum honeycomb was $60 \times 0.1 \times 30\ mm^3$ (length × width × height). Additionally, the physical property parameters used in the simulation are shown in Table 1.

2.2. Governing Equations and Boundary Conditions. The boundary conditions of the inlet and outlet were set as velocity–inlet and pressure–outlet, respectively. The thermal contact resistance should be neglected owing to its high heat transfer efficiency inside of the device. The inlet water temperature was equal to ambient temperature, as shown in Figure 2, where air entered (inlet) with a certain velocity at the right and left (outlet) at the left.

There were two main heat transfer models in this study, and the heat transfer in solids was given by the diffusion equation as follows:

$$\rho c_p \frac{\partial T}{\partial t} = \nabla \bullet (k \nabla T) + \dot{Q}, \tag{1}$$

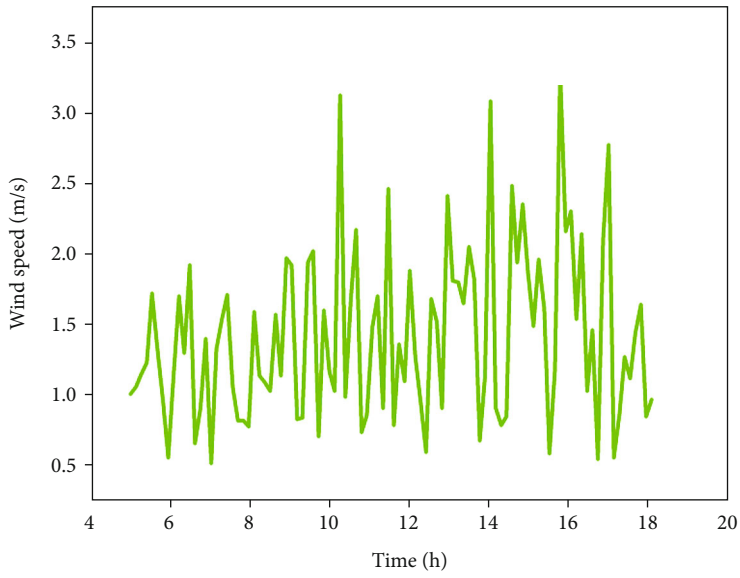

(a)

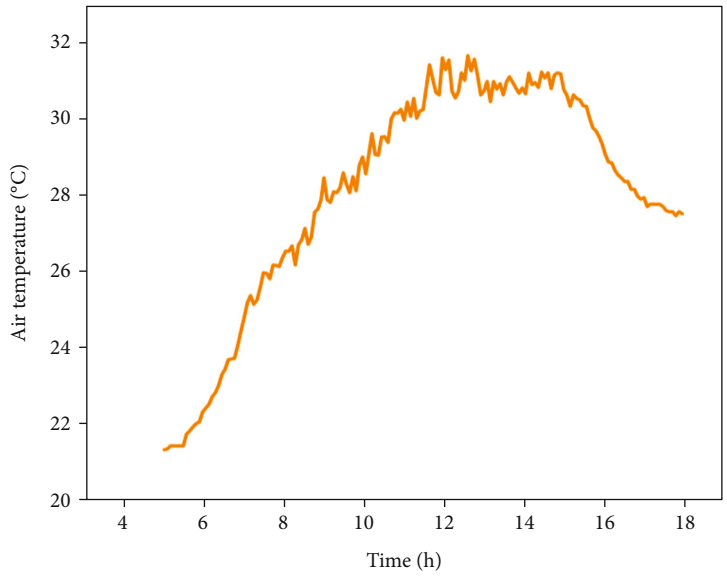

(b)

Figure 3: Continued.

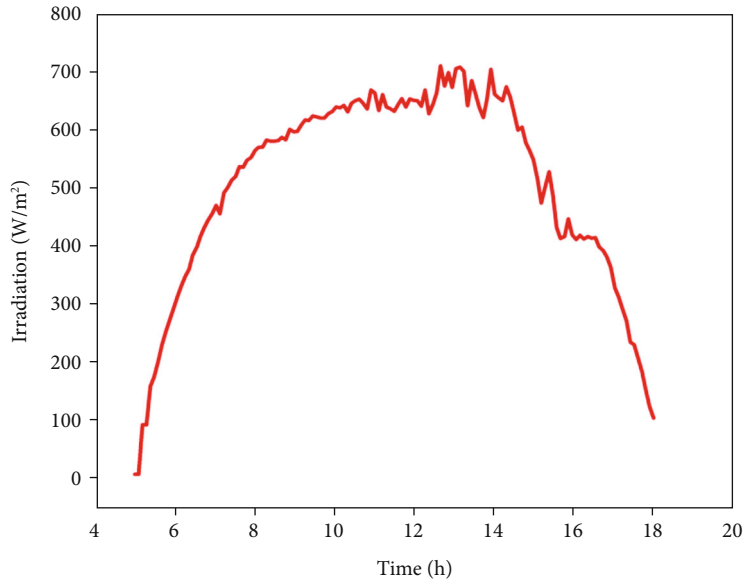

(c)

Figure 3: Initial weather data: (a) wind speed, (b) air temperature, and (c) irradiation intensity.

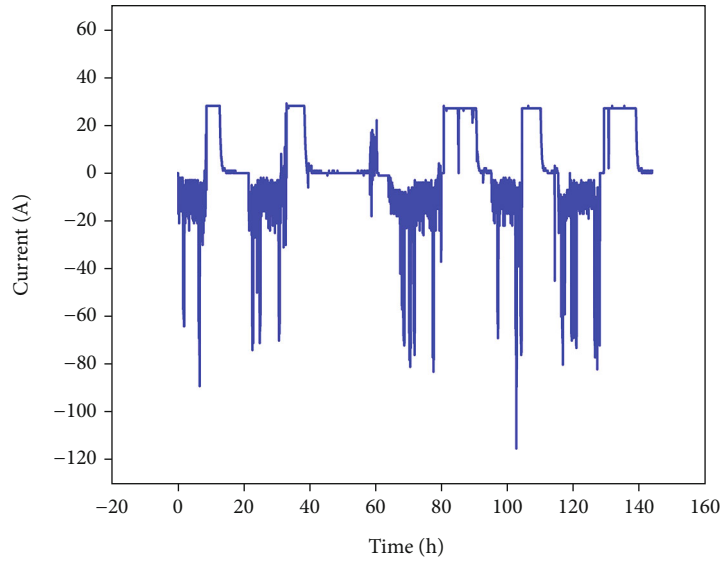

Figure 4: The current of the PV energy storage system.

where k was the thermal conductivity ($W{\cdot}m^{-1}{\cdot}k^{-1}$), T stood for temperature vector, $\dot{Q}$ was heat generation rate (W), ρ was density ($kg{\cdot}m^{-3}$), c_p was specific heat ($J{\cdot}kg^{-1}{\cdot}k^{-1}$), and t was time (s). And Equation (1) is applied to the PV module, the batteries, the controller, the junction box, and the PCM.

The heat transfer in fluids was calculated using

$$\rho c_p \frac{\partial T}{\partial t} + \rho c_p (u \nabla T) = \nabla \bullet (k \nabla T) + \dot{Q}, \quad (2)$$

where u presented the velocity vector of air.

Table 2: Technical parameters of the retired $LiFePO_4$ power batteries.

Items	Technical parameters
Nominal voltage/capacity (V/Ah)	3.2/20
Cutoff voltage of charge (V)	3.65
Cutoff voltage of discharge (V)	2.0
Max charge current (A)	100
Max discharge current (A)	100
Size (mm)	152 × 120 × 22
Operating temperature range (°C)	25–50

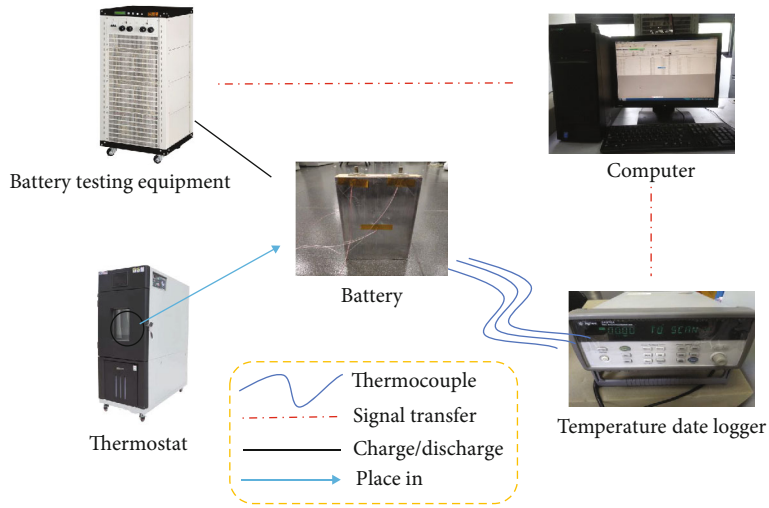

Figure 5: Battery heat production test experimental platform.

The momentum conservation equation for air was as follows:

$$\mu\nabla^2 - \nabla p = \rho(u \bullet \nabla T) + \rho\frac{\partial u}{\partial t}. \quad (3)$$

The continuity equation for air was given by

$$\nabla \bullet u = 0, \quad (4)$$

where μ stood for viscosity and p for pressure in all directions. Equation (2) and (3) were completely coupled since both equations include the velocity term u.

The irradiance (G) would cause heat generation of the glass layer and the silicon layer of PV module. The glass layer generates little heat, which had a small impact on the overall calculation and could be ignored. Hence, the heat production of the silicon layer in the PV module was only considered in this study. The contribution of the heat generated in the silicon layer was defined as follows [31]:

$$Q_{si} = \frac{G(1-R)\left(1-A_{glass}\right)\left(1-\eta_{PV}\right)}{t_{si}}, \quad (5)$$

where $R = 7\%$ was the reflectivity of glass layer, A_{glass} was glass area, $\eta_{PV} = 0.162$ was efficiency of PV panel, and t_{si} was silicon layer thickness.

2.3. Input Environment Data. In order to improve the authenticity of the research, the data of the Shunde Sun Yat-sen University Institute for Solar Energy (N 22°54′27.55″, E 113°12′1.22″) were selected. The data of wind speed, air temperature, and irradiation from 5 am to 18 pm were recorded from the first day to the sixth day, as shown in Figure 3. Besides, the current of the PV energy storage system for six consecutive days was detected, which are shown in Figure 4. The significance of the data in Figure 4 is to obtain the heat production of the battery in the subsequent in order to ensure more accurate original input data of the simulation.

Table 3: Heat production rate of $LiFePO_4$ batteries at different discharge rates.

Discharge rate (C)	1.0	1.5	2.0	3.0	4.0	5.0
Heat production (W)	1.26	12.77	14.42	25.81	132.37	212.49

2.4. Thermal Behaviors of Power Batteries. In order to verify the feasibility of decommissioned power batteries that have been retired from EVs/HEVs after two years of use, some decommissioned lithium iron phosphate power batteries (3.2 V/20 Ah) of the same batch were selected for experimental research. It is worth noting that the technical parameters of the retried batteries were described in Table 2. The schematic diagram of the experimental platform for heat generation testing is shown in Figure 5. To measure the heat generation behaviors of the battery during charging and discharging electrochemical reaction processes, a battery was enclosed in a thermostat (BTH–800, Dongguan Bell Co. Ltd., China) maintaining a constant ambient temperature of 30°C. The temperature variations of the battery were collected by a temperature acquisition instrument (Agilent 34970 A, Agilent Technologies Inc. China) through connecting with thermocouples (OMEGA type TT–T–30–SLE–1 M, Norwalk, CT, USA; accuracy of ±0.1°C). Besides, the charge and discharge experiments were carried out by employing a battery testing equipment (BTS–50 V/120 A–NTF, Shenzhen Neware Electronics Co. Ltd., China). From Table 3, the heat production behaviors of aforementioned power batteries at different discharge rates could be obtained.

As described in Figure 5, both of the data logger and battery testing equipment were connected with a computer. The

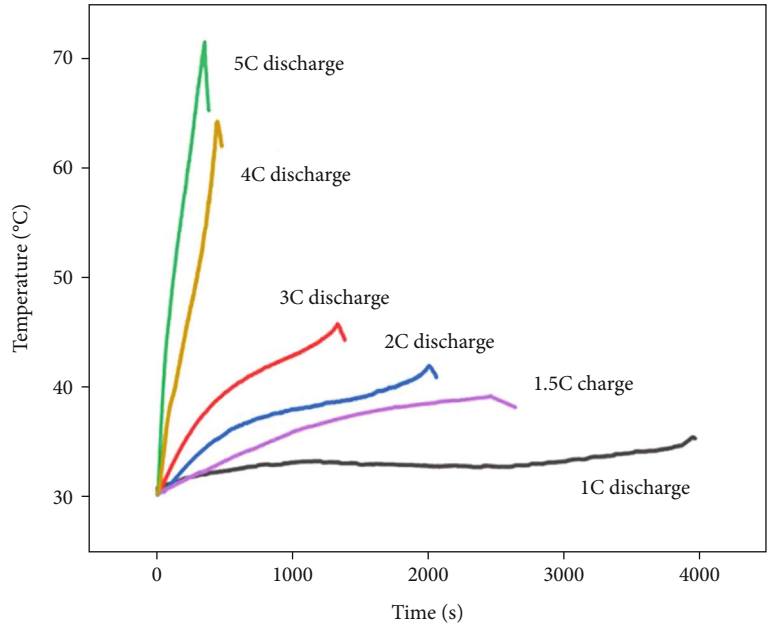

(a)

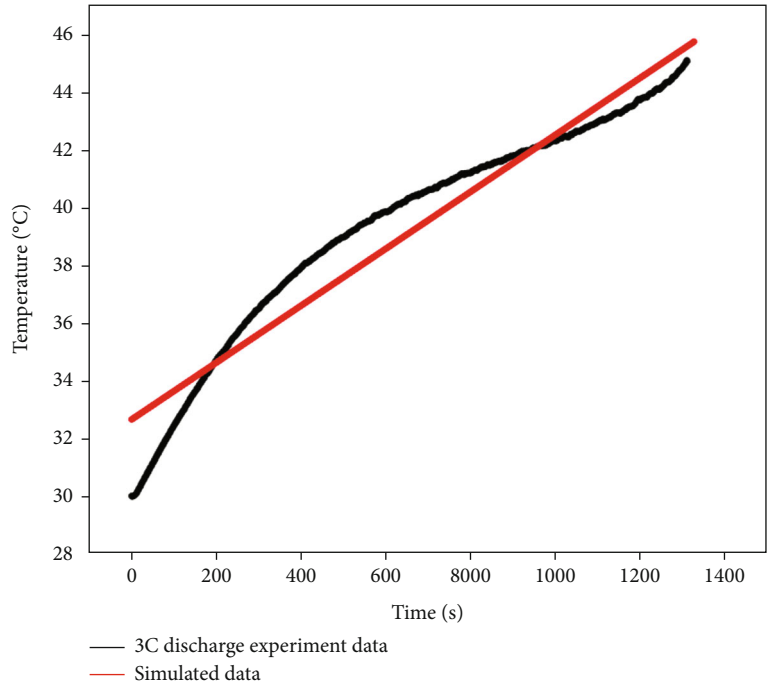

(b)

Figure 6: Continued.

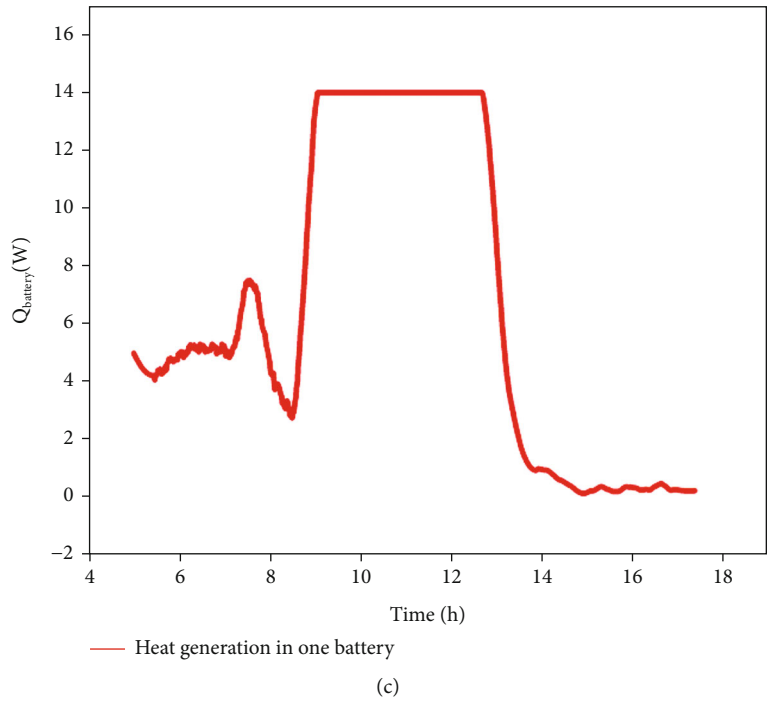

(c)

Figure 6: Battery heat generation behaviors: (a) experiment data, (b) simulated data, and (c) input data.

battery was conducted for 1.5 C high-rate charge experiment and discharged at 1.0 C, 2.0 C, 3.0 C, 4.0 C, and 5.0 C rates, respectively and the temperature variations are shown in Figure 6(a). Figure 6(b) presents the average temperature of the battery when discharged at 3.0 C rate and the $T \sim t$ curve fitted by the polynomial method. The fitting formula can be expressed as follows:

$$T = at + b, \tag{6}$$

$$\frac{d_T}{d_t} = a. \tag{7}$$

In the formula, $a = 0.00985$, $b = 31.645$, T was the average temperature of the battery at 3 C discharge rate, and t is the discharge time. Then, the average heat generation rate of the battery at 3 C discharge rate could be expressed as follows:

$$q_{3C} = C_p ma \approx 25.81 \text{ W}. \tag{8}$$

3. Results and Discussions

Three types of PBIS containing of G–PBIS, H–PBIS, and HP–PBIS were studied in this research. Considering the higher ambient temperature in the daytime than the night, furtherly affecting the battery in the PBIS, this research focused on the temperature changes of the PBIS when there was solar radiation during the specific time period of the day: from 5 am to 18 pm, and the research time range converted into the transient model was 0–46800 s.

3.1. Independence Test of Grid Number. To make sure the calculation accuracy of the transient simulation, the independence test of grid number was performed. As presented in Figure 7(a), the temperature of the middle face of the two batteries in 40000 s was used to measure the independence of the grid number, and the testing results are exhibited in Figure 7(b). When the grid number increased from 465094 to 1710940, the temperature variation rate was only 0.076%. Hence, the grid number of 465094 was utilized in this study.

3.2. Temperature Analysis of G–PBIS. As shown in Figure 8, in order to study the changes of the internal temperature of G–PBIS under the natural environment condition, the temperature nephograms at 15000 s, 25000 s, 35000 s, and 45000 s were selected as representatives. It should be known that the highest temperature zone at the G–PBIS usually changed from PV panel to the battery areas. In order to further illustrate the temperature changes inside the G–PBIS, the temperatures of the points $P_{si1} - P_{si7}$ described in Figure 9(a) were taken in the silicon layer of the G–PBIS, and the temperature measuring results are shown in Figure 9(b). Additionally, the temperature point arrangement of the eight upper surfaces $P_{b1} - P_{b8}$ and one lower surface P_{b9} of the battery are described in Figure 9(c), and the temperature curves are shown in Figure 9(d). From Figure 9(b), it could be seen that the

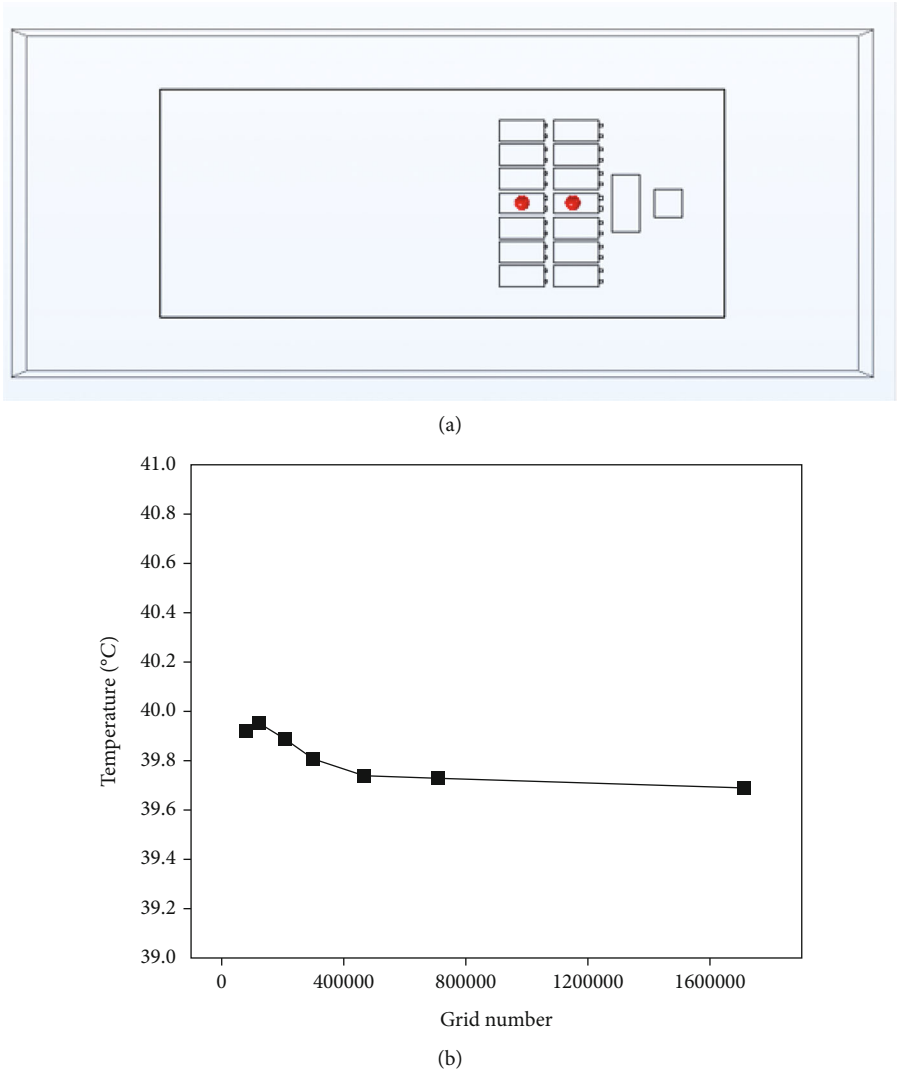

Figure 7: Details and results of grid independence tests: (a) detection point diagram and network and (b) independence verification results.

maximum temperature of the silicon layer in a day reached 84.95°C, and the maximum temperature difference was maintained within 24.82°C. The working efficiency of solar cells would decrease as the temperature increased. At the same time, due to the thermal expansion properties of the material, the existence of temperature differences also led to the generation of internal thermal stress in PV modules, which furtherly accelerated the aging and performance degradation of PV modules. Simultaneously, it could be observed that the maximum temperature of the battery also reached the maximum value of 87.93°C, and the maximum temperature difference came to 17.96°C. This would greatly reduce the operating performance and shorten the service life of lithium–ion batteries with an operating temperature range of 25–50°C. What was more, high temperature would easily give rise to thermal runaway (TR). Therefore, in order to assure the device more secure and durable, exploring an effective structure and design for PBIS for controlling its internal temperature and stretching the temperature distribution is very necessary.

3.3. Temperature Analysis of H–PBIS. The temperature contours of the H–PBIS at 15000 s, 25000 s, 35000 s, and 45000 s are shown in Figure 10. It could be seen that the temperature of the H–PBIS was obviously lower than that of the G–PBIS after laying out the aluminum honeycomb. At the same time, the highest temperature area inside the H–PBIS could be also gathered to the batteries. Around the battery array, it could be obviously seen that the high thermal conductivity of aluminum honeycomb reduced the internal temperature of the PBIS to a certain degree. Moreover, the battery temperature variations of H–PBIS were also collected. As could be seen in Figure 11, the maximum battery temperature of H–PBIS reached 78.48°C, and the maximum temperature difference was decreased to 16.36°C, which was obviously lower than that of G–PBIS.

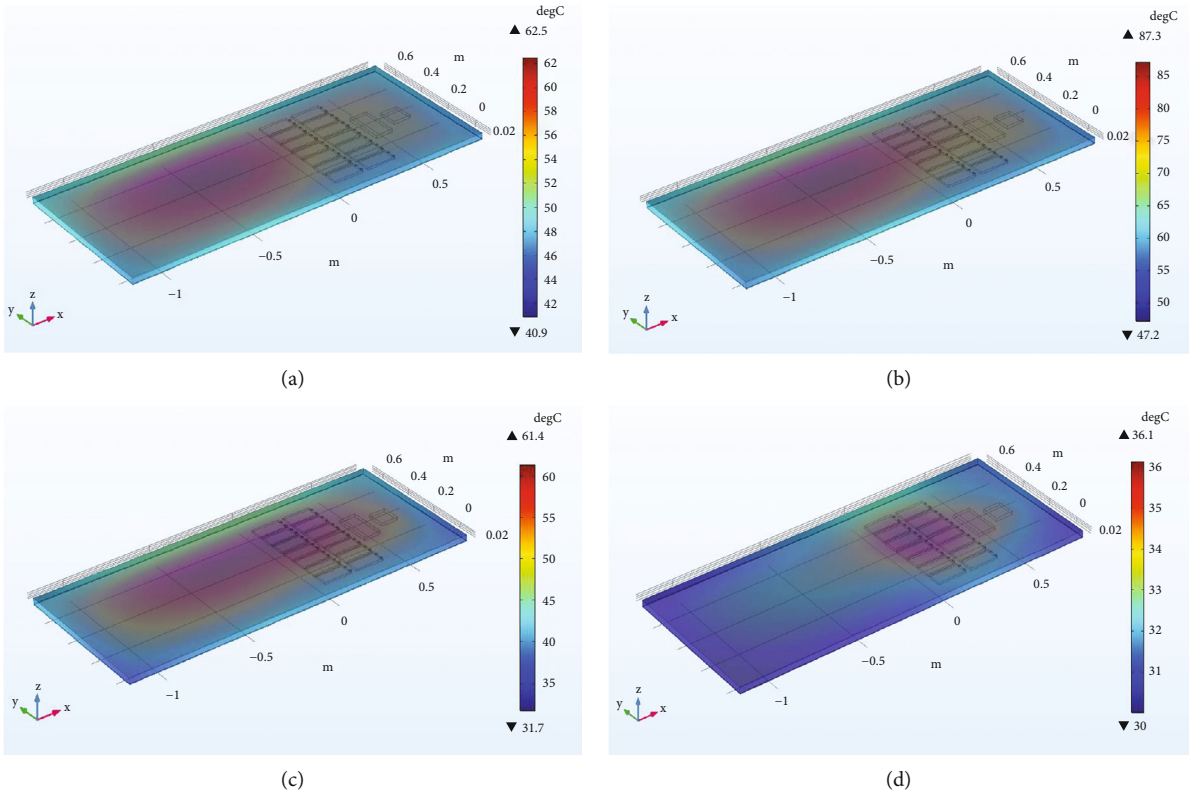

Figure 8: Temperature contours of G–PBIS under air convection mode: (a) 15000 s, (b) 25000 s, (c) 35000 s, and (d) 45000 s.

Nevertheless, in order to obtain more excellent thermal management effect, the structure of aluminum honeycomb was valuable and worthy for improving furtherly. The H–PBISs with various side lengths such as 45 mm, 75 mm, 90 mm, and 105 mm were designed, respectively. In addition, the thickness and height of the aluminum honeycomb were also maintained at 0.1 mm and 30 mm, respectively. As the operating conditions of the H–PBIS with a side length of 60 mm, the temperature cloud diagrams had been taken at 25000 s. As shown in Figure 12, the maximum temperatures reached 78.9°C, 78.5°C, 77.4°C, 75.6°C, and 76.5°C, when the side lengths of aluminum honeycombs are 45 mm, 60 mm, 75 mm, 90 mm, and 105 mm, respectively. It showed that the temperature of the H–PBIS gradually decreased as there is an increase of the side length of the aluminum honeycomb. Surprisingly, it rose when it came to the highest value of 105 mm. Thus, it could be concluded that 90 mm was the optimal side length design of H–PBIS. However, the maximum temperature of battery in H–PBIS still reached a relative temperature of 75.6°C with 90 mm aluminum honeycomb side length, which would bring out severe safety issues and risks for lithium–ion batteries. Thus, it is essential to design a more efficient heat dissipation approach to make the battery module operating within a reasonable temperature range.

3.4. Temperature Analysis of HP–PBIS. Considering the particular advantages of PCM, such as high latent heat, low cost, and suitable phase transition temperature, it was selected and utilized for absorbing the heat generated from the battery module in the device. The battery module was designed and investigated with three different types of PCM (melting point: 35–45°C; latent heat: 165 J/g; thermal conductivity: 1.5 W/m·k) for thermal management, including single layer with the size of $5 \times 165 \times 75\ mm^3$; single layer, $10 \times 165 \times 75\ mm^3$; and double layers, $10 \times 165 \times 75\ mm^3$. The above-mentioned composite PCMs are composed of 78% paraffin, 5% expanded graphite, 5% flame retardant, and 12% polyethylene glycol. What is worth noting is that the thickness and volume of the PCM are determined by the size of the battery, the heat generation of the PCM battery, and the thickness of the photovoltaic module.

As shown in Figure 13, H–PBIS coupled with three types of PCM structures were marked as HP–PBISa, HP–PBISb, and HP–PBISc, respectively. The temperature cloud diagrams of the aforementioned three structures at the time of 25000 s are described in Figures 13(d)–13(f), respectively. Testing results indicated that the highest temperatures of HP–PBISa, HP–PBISb, and HP–PBISc were 68.3°C, 64.7°C, and 58.1°C, respectively, which were lower than the lowest temperature (75.6°C) of H–PBIS at 25000 s. It could be concluded that compared with H–PBIS with single aluminum honeycomb structure, the honeycomb–PCM coupling structure played a vital role in slowing down the temperature rising rate.

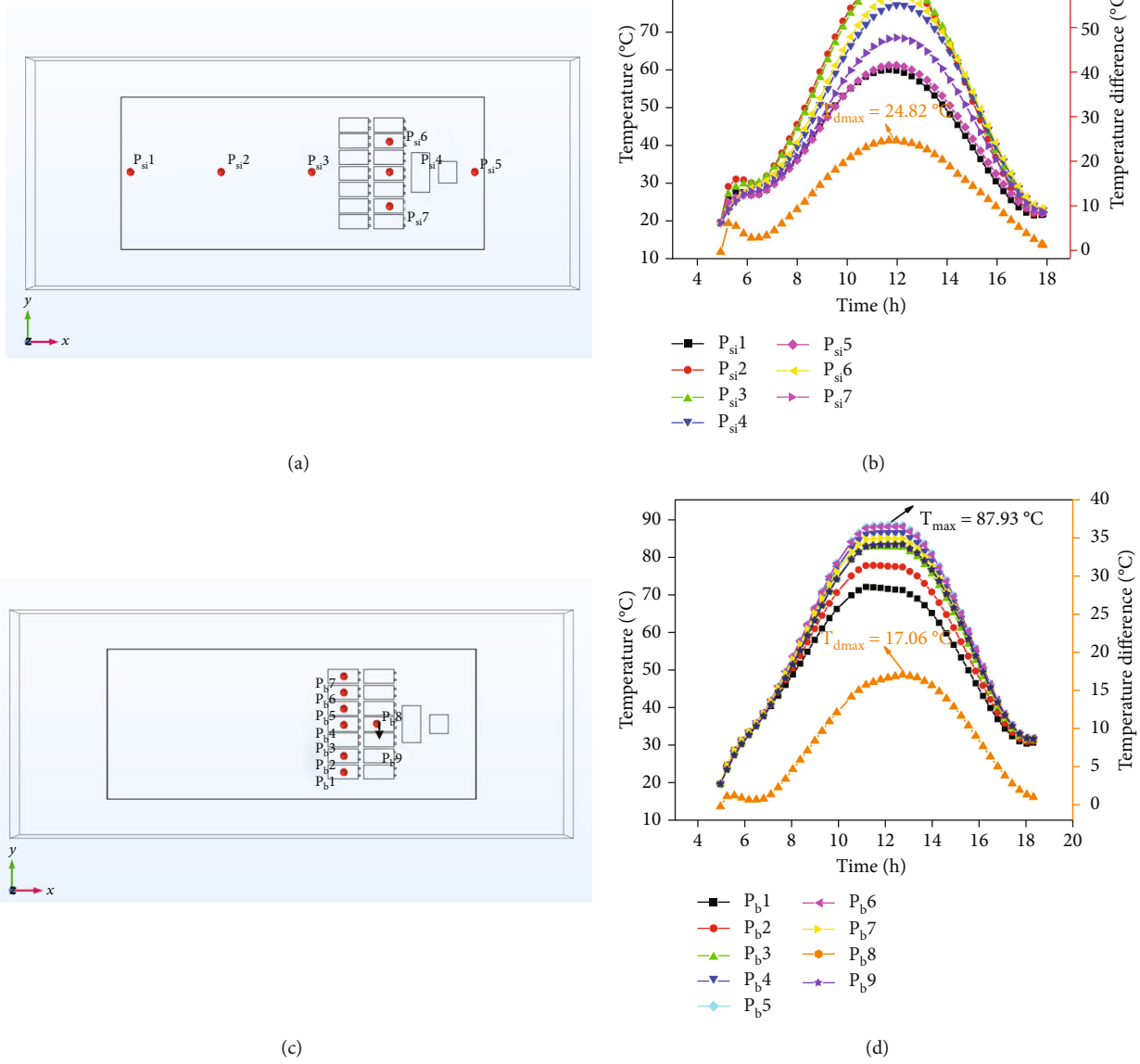

FIGURE 9: Schematic and measuring results of G–PBIS: (a) detection point diagram of silicon layer in G–PBIS, (b) temperature variations of silicon layer in G–PBIS, (c) detection points distribution of batteries in G–PBIS, and (d) temperature variations of batteries in G–PBIS.

The temperature changes of the maximum temperature points of the batteries among the three types of HP–PBIS are exhibited in Figure 14(a). When the temperature increased to 35°C, the PCM started to change from solid to liquid, and most of the heat generated by the battery was absorbed by the PCM in the form of latent heat, effectively reducing the battery temperature rise gradient and controlling the peak temperature. As could be seen from Figure 14(a), the maximum temperatures of the internal batteries of HP–PBISa, HP–PBISb, and HP–PBISc were 69.11°C, 65.42°C, and 53.72°C, respectively. Besides, the temperature changes of the internal batteries and the maximum temperature difference in HP–PBISc are also analyzed in Figure 14(b), the maximum temperature was 53.72°C, and the maximum temperature difference was 8.34°C, which were obviously lower than that of the G–PBIS and H–PBIS. These corresponding results furtherly confirmed that H–PBIS coupling with PCM would greatly improve thermal performance.

3.5. Validation of the Simulation Model. In this section, referring to the research results of numerical simulation, three sets of testing experiments were carried out. As shown in Figure 15, two retired lithium iron phosphate power batteries with a nominal capacity of 20 Ah and 50% SOC were connected in series. Then, we attached

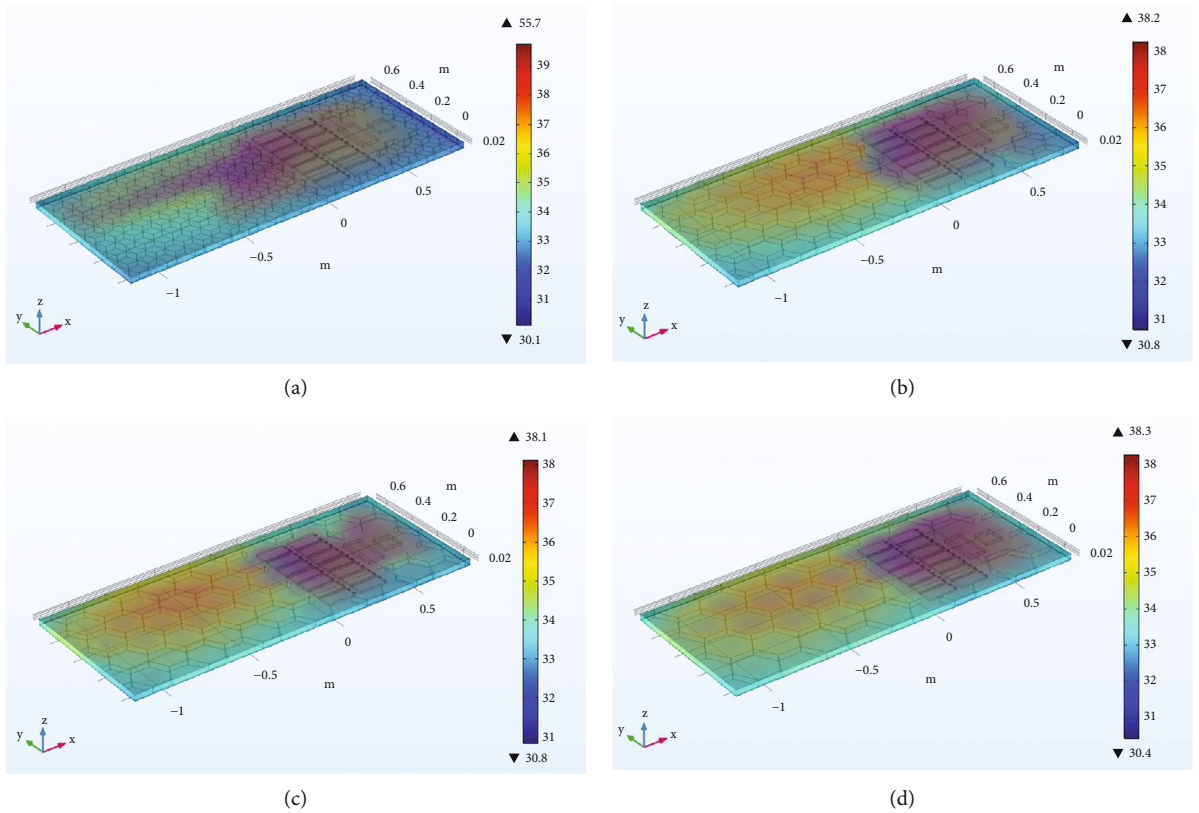

Figure 10: Temperature contours of H–PBIS under air convection condition: (a) 15000 s, (b) 25000 s, (c) 35000 s, and (d) 45000 s.

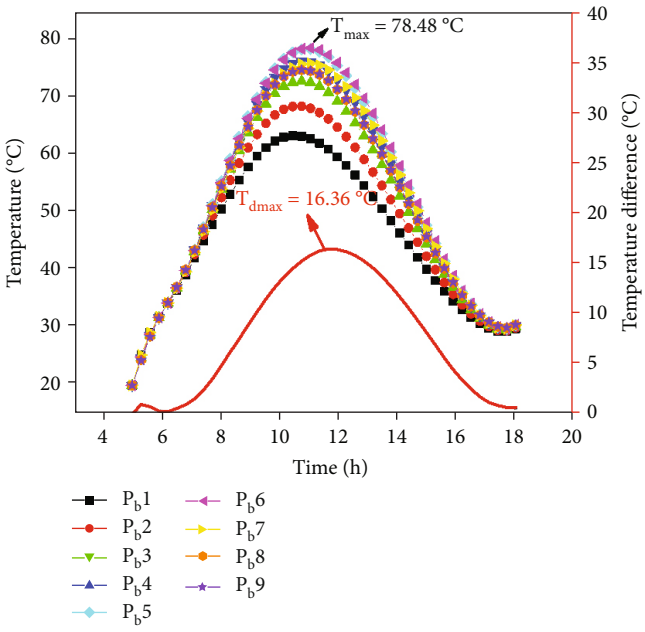

Figure 11: Temperature variations of battery in H–PBIS.

the thermal conductive silica gel for the battery to the aluminum plate, referred to the G–PBIS model and named it PBIS–a. After that, on the basis of PBIS–a, some aluminum honeycomb structures were added to fill the space except the battery and the junction box, which was PBIS–b. Next, based on PBIS–b, adding two PCM plates (thermal conductivity: 1.65 W/(m·k); latent heat: 153.19 J/g) to the upper and lower surfaces of each battery, which was named PBIS–c. After the aluminum plate assembly was finished, the polycrystalline PV module with a rated power of 50 W was connected to one end of the solar controller with maximum power point tracking. Simultaneously, the other end of the solar charge controller was connected in series with the battery, and then two thermocouples were connected to the front and back of the selected battery.

After connecting all the components and measuring equipment, three PV energy storage integrated systems were placed under a small solar simulator, which generated a constant radiation of 400 W, and then tested under the ambient temperature of 20°C.

After an hour of testing, the lighting simulator was turned off and the infrared camera images of each experimental group were recorded at the end. As shown in Figure 16, the highest point temperature of PBIS–a, PBIS–b, and PBIS–c reached 42.9°C, 41.2°C, and 38.0°C, respectively. The average temperature changing curves of the two battery surfaces are exhibited in Figure 17. As

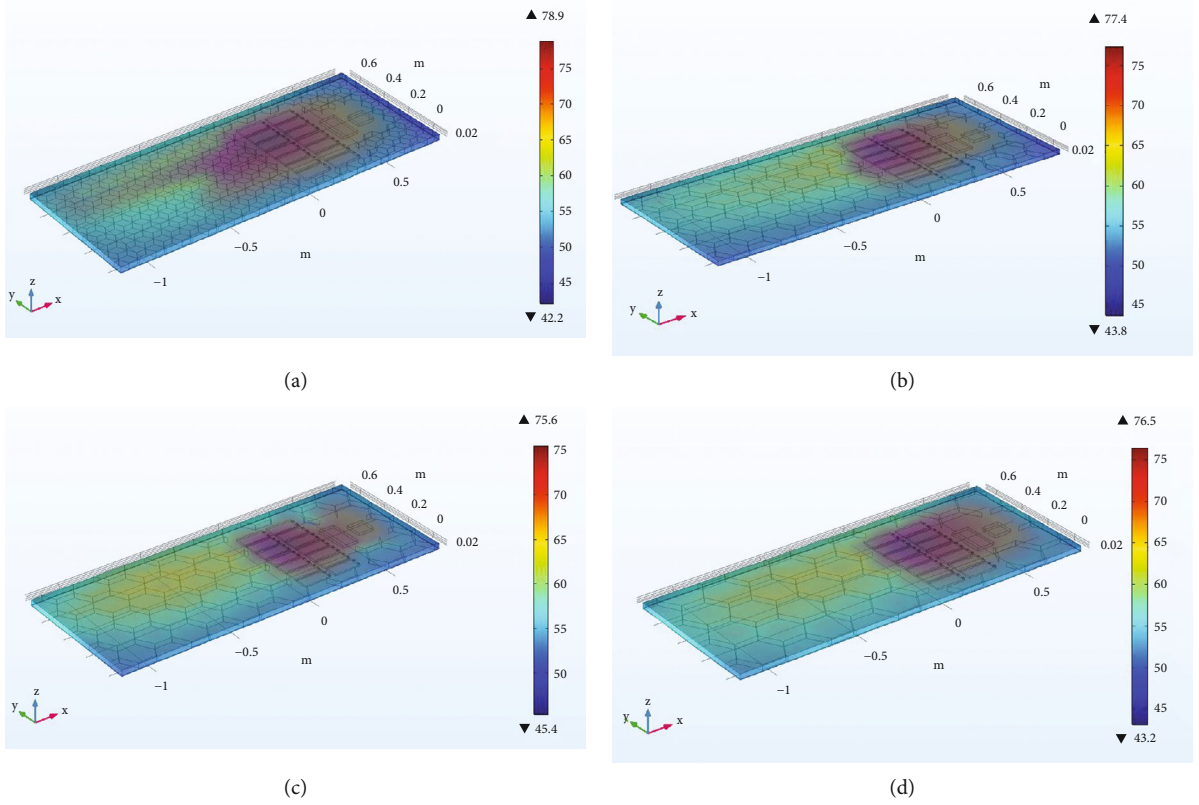

Figure 12: Temperature contours of H–PBIS with different side lengths of aluminum honeycomb: (a) 45 mm, (b) 75 mm, (c) 90 mm, and (d) 105 mm under air convection condition at 25000 s.

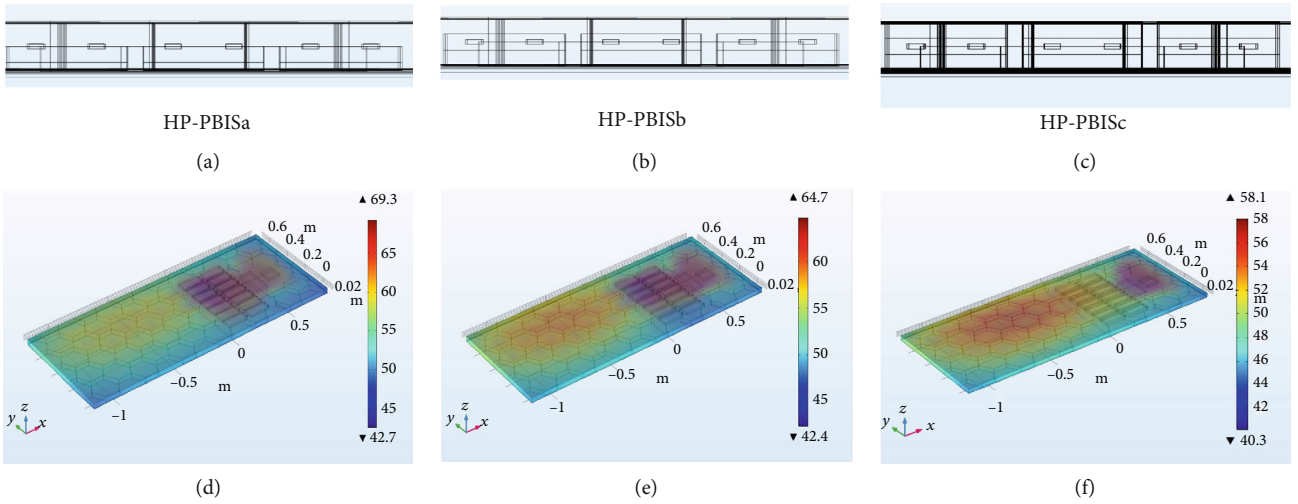

Figure 13: Structural model diagrams: (a) single layer—$5 \times 165 \times 75\,mm^3$, (b) single layer—$10 \times 165 \times 75\,mm^3$, and (c) double layers—$10 \times 165 \times 75\,mm^3$; and temperature contours of (d) HP–PBISa, (e) HP–PBISa, and (f) HP–PBISa under air convection mode at 25000 s.

expected from the results of the numerical model, the experimental group integrating the PCM and the aluminum honeycomb presented a lower temperature and a slower temperature rise gradient, finally exhibiting the outstanding heat dissipation effectiveness under the same light conditions, ambient temperature, and natural convection environment. This result further verified that the combination of aluminum honeycomb and PCM could play a significant role in controlling the temperature rise of the PBIS.

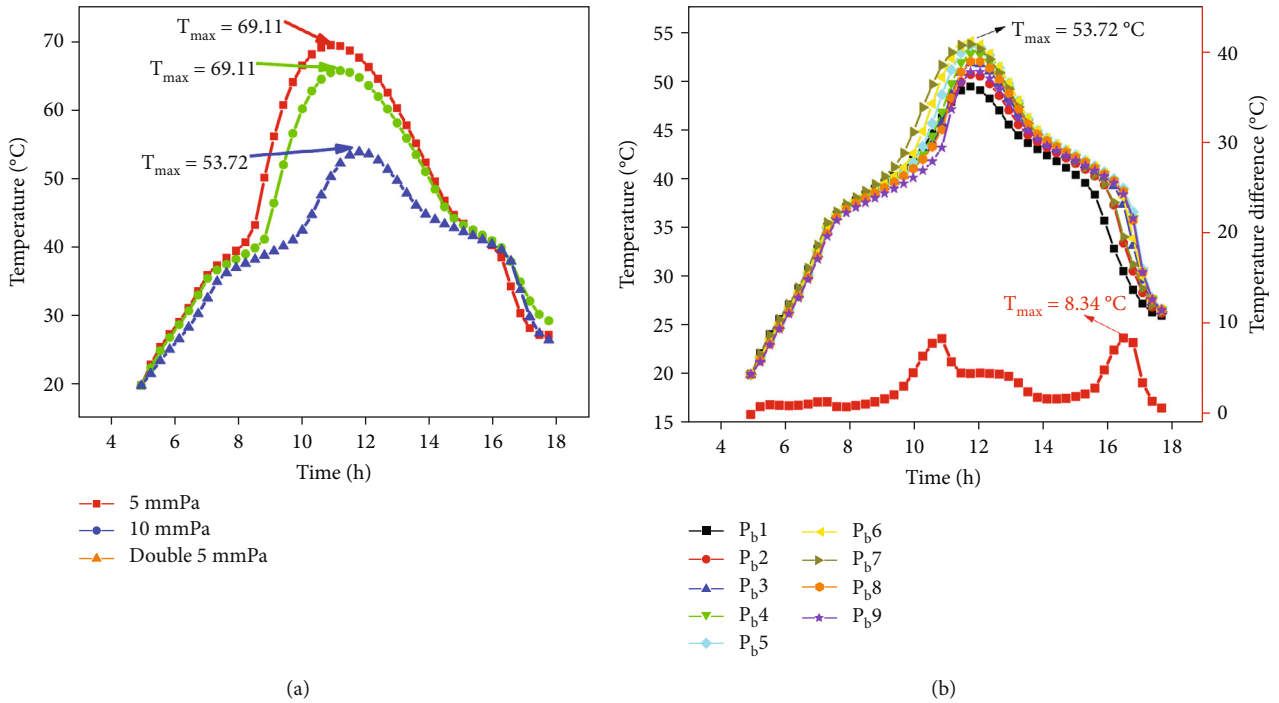

(a) (b)

Figure 14: Analysis of heat generation behaviors: (a) temperature variations of batteries in three types of HP–PBIS and (b) temperature variations and temperature difference of battery in HP–PBISc.

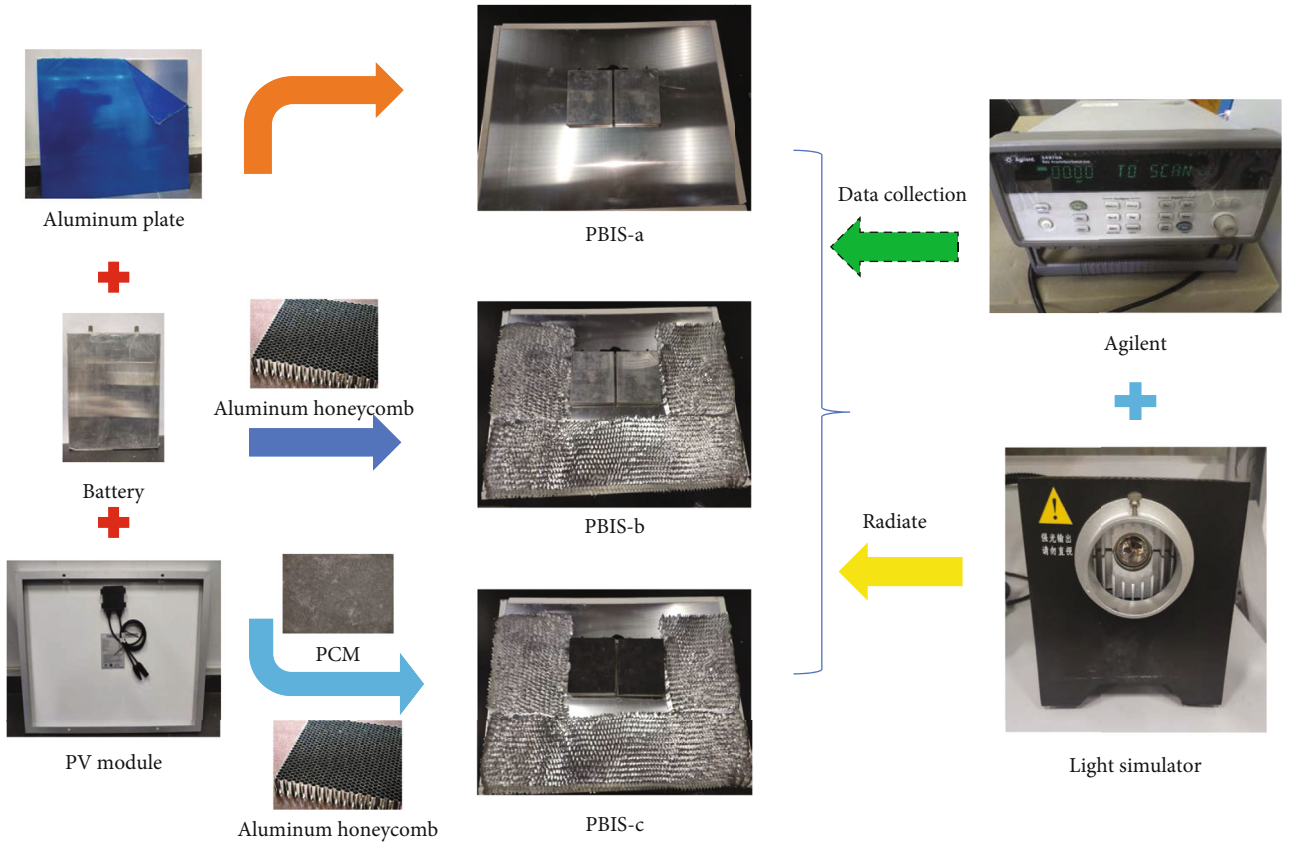

Figure 15: Model construction of PV–battery integrated system.

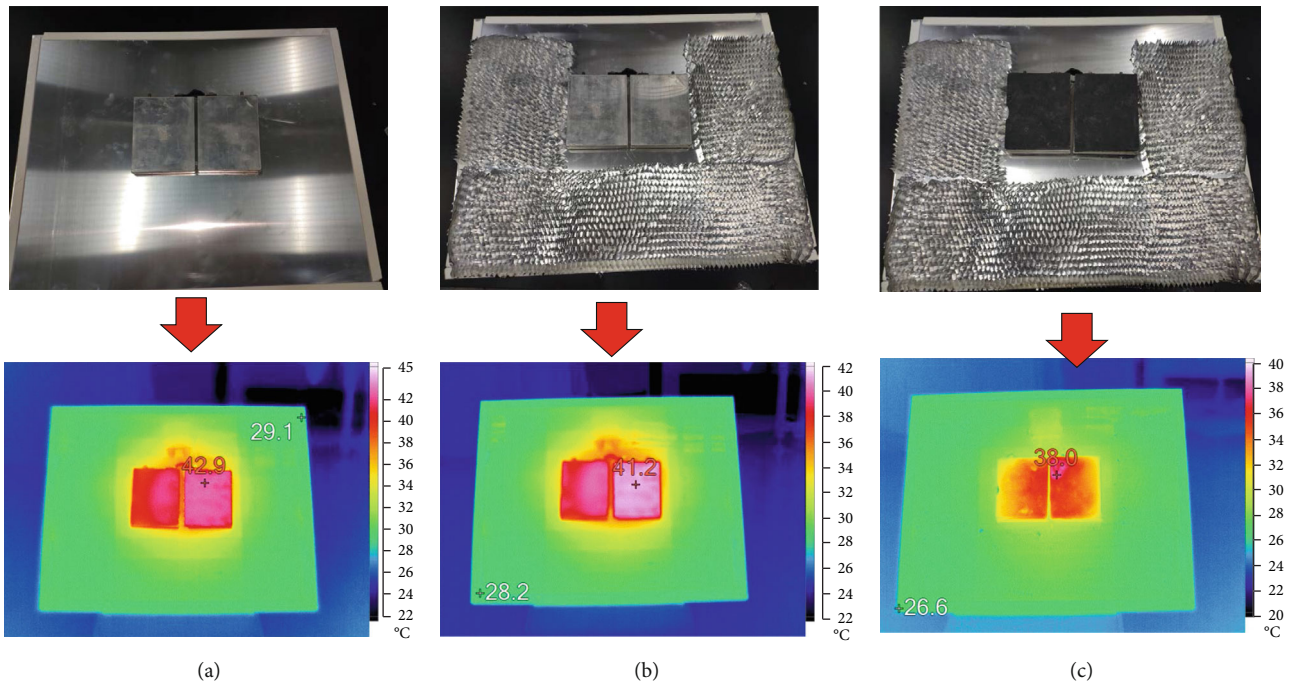

Figure 16: Infrared camera images after one hour of illumination: (a) PBIS–a, (b) PBIS–b, and (c) PBIS–c.

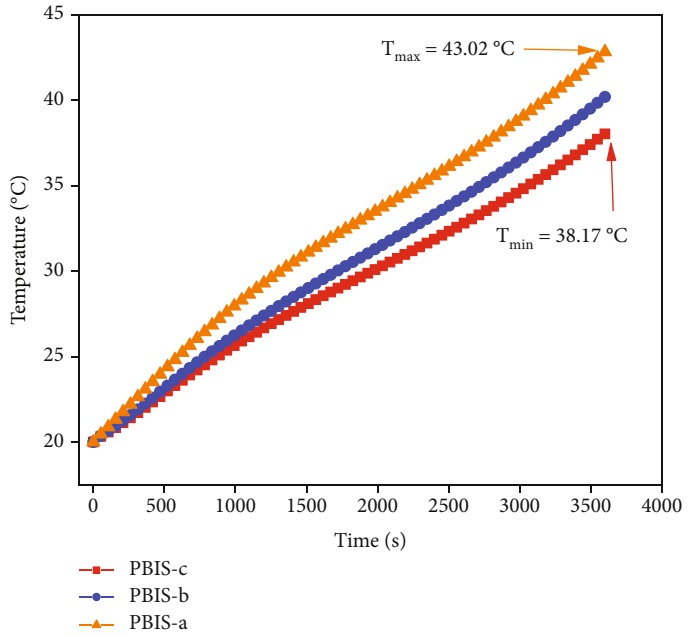

Figure 17: Average temperature rise of the battery in PBIS–a, PBIS–b, and PBIS–c systems after one hour of illumination.

4. Conclusions

The integration system of solar energy and lithium ion battery without any extra control electronics attracted much attention, which was regarded as a compact and longtime service solution for portable electronic devices and energy storage fields. In this paper, three finite element models of PV–battery integrated systems containing of G–PBIS, H–PBIS, and HP–PBIS were particularly proposed and investigated. For G–PBIS, the maximum temperature of the battery reached 87.93°C. For comparison, the maximum temperature of the battery in H–PBIS filled with 90 mm aluminum honeycomb came to 78.48°C. In order to further reduce the battery temperature, a structural model of the battery coupling with PCM was developed. The results revealed that the maximum temperature of the HP–PBISc battery

combining with the double layer $10 \times 165 \times 75\,mm^3$ PCM was decreased to 53.72°C. Compared with G–PBIS, the maximum temperature of HP–PBISc was decreased to 34.21°C. Moreover, the temperature consistency was greatly promoted with the peak temperature difference reducing from 17.06°C to 8.34°C. Hence, it could be concluded that the optimum PV–battery integrated system could not only maintain the battery module within a relative suitable operating temperature range but also provide an effective and feasible system for renewable energy solution in practical application.

Data Availability

The data used to support the findings of this study are available from the corresponding author upon request.

Conflicts of Interest

The authors declare that they have no conflicts of interest.

Acknowledgments

This research was financially supported by the Guangdong Key Laboratory of Battery Safety (Grant No. 2019B121203008), the National Natural Science Foundation of China (Grant No. 51906047), and Zhuhai Science and Technology Project (2H2203620121015PWC).

References

[1] X. Mei, P. Xie, and B.-C. Xie, "Study of China's optimal solar photovoltaic power development path to 2050," *Resources Policy*, vol. 65, p. 101541, 2020.

[2] M. H. Alaaeddin, S. M. Sapuan, M. Y. M. Zuhri, E. S. Zainudin, and F. M. al- Oqla, "Photovoltaic applications: status and manufacturing prospects," *Renewable and Sustainable Energy Reviews*, vol. 102, pp. 318–332, 2019.

[3] G. Angenendt, M. Merten, S. Zurmühlen, and D. U. Sauer, "Evaluation of the effects of frequency restoration reserves market participation with photovoltaic battery energy storage systems and power-to- heat coupling," *Applied Energy*, vol. 260, p. 114186, 2020.

[4] S. U.-D. Khan, Z. A. Almutairi, O. S. al-Zaid, and S. U.-D. Khan, "Development of low concentrated solar photovoltaic system with lead acid battery as storage device," *Physics*, vol. 20, no. 4, pp. 582–588, 2020.

[5] H. Akbari, M. C. Browne, A. Ortega et al., "Efficient energy storage technologies for photovoltaic systems," *Solar Energy*, vol. 192, pp. 144–168, 2019.

[6] J. Liu, X. Chen, H. Yang, and Y. Li, "Energy storage and management system design optimization for a photovoltaic integrated low-energy building," *Energy*, vol. 190, p. 116424, 2020.

[7] R. Chaurasia, S. Gairola, and Y. Pal, "Technical, economic feasibility and sensitivity analysis of solar photovoltaic/battery energy storage off-grid integrated renewable energy system," *Energy Storage*, vol. 4, p. 283, 2021.

[8] M. Li, H. Deng, Y. Zhang, and C. Hou, "A small hybrid power system of photovoltaic cell and sodium borohydride hydrolysis-based fuel cell," *Micromachines*, vol. 12, no. 3, p. 278, 2021.

[9] F. Fang, Z. Zhu, S. Jin, and H. Shiyan, "Two-layer game theoretic microgrid capacity optimization considering uncertainty of renewable energy," *IEEE Systems Journal*, vol. 15, no. 3, pp. 4260–4271, 2021.

[10] S. N. Agbo, T. Merdzhanova, S. Yu et al., "Development towards cell-to-cell monolithic integration of a thin-film solar cell and lithium-ion accumulator," *Journal of Power Sources*, vol. 327, pp. 340–344, 2016.

[11] W. Grzesiak, P. Mackow, T. Maj et al., "Innovative system for energy collection and management integrated within a photovoltaic module," *Solar Energy*, vol. 132, pp. 442–452, 2016.

[12] V. Vega-Garita, L. Ramirez-Elizondo, and P. Bauer, "Physical integration of a photovoltaic-battery system: A thermal analysis," *Applied Energy*, vol. 208, pp. 446–455, 2017.

[13] J. Zhang, D. Shao, L. Jiang et al., "Advanced thermal management system driven by phase change materials for power lithium-ion batteries: a review," *Renewable and Sustainable Energy Reviews*, vol. 159, p. 112207, 2022.

[14] M. M. Awad, O. K. Ahmed, O. M. Ali et al., "Photovoltaic Thermal Collectors Integrated with Phase Change Materials: A Comprehensive Analysis," *Electronics*, vol. 11, no. 3, p. 337, 2022.

[15] S. Bouadila, M. Lazaar, S. Skouri, S. Kooli, and A. Farhat, "Energy and exergy analysis of a new solar air heater with latent storage energy," *International Journal of Hydrogen Energy*, vol. 39, no. 27, pp. 15266–15274, 2014.

[16] A. E. Kabeel, A. Khalil, S. M. Shalaby, and M. E. Zayed, "Experimental investigation of thermal performance of flat and v-corrugated plate solar air heaters with and without PCM as thermal energy storage," *Energy Conversion and Management*, vol. 113, pp. 264–272, 2016.

[17] A. El Khadraoui, S. Bouadila, S. Kooli, A. Guizani, and A. Farhat, "Solar air heater with phase change material: An energy analysis and a comparative study," *Applied Thermal Engineering*, vol. 107, pp. 1057–1064, 2016.

[18] T. Thomas and G. Tiwari, "Energy absorption and in-plane crushing behavior of aluminium reinforced honeycomb," *Vacuum*, vol. 166, pp. 364–369, 2019.

[19] C. Ana, "Thermo-mechanical stability of lightweight glass-free photovoltaic modules based on a composite substrate," *Solar Energy Materials & Solar Cells*, vol. 187, pp. 82–90, 2018.

[20] Z. Gao, Y. Zhang, N. Song, and X. Li, "Biomass-derived renewable carbon materials for electrochemical energy storage," *Mater. Res. Lett.*, vol. 5, no. 2, pp. 69–88, 2017.

[21] X. Li, Q. Huang, and G. Zhang, "Evaluation of lithium battery thermal management using sealant made of boron nitride and silicone," *Journal of Power Sources*, vol. 451, p. 227820, 2020.

[22] Y. Zhu, Z. Wang, and L. H. Poh, "Auxetic hexachiral structures with wavy ligaments for large elasto-plastic deformation," *Smart Materials & Structures*, vol. 27, no. 5, p. 055001, 2018.

[23] M. Abuska, S. Sevik, and A. Kayapunar, "A comparative investigation of the effect of honeycomb core on the latent heat storage with PCM in solar air heater," *Applied Thermal Engineering*, vol. 148, pp. 684–693, 2019.

[24] C. Hasse, M. Grenet, A. Bontemps, R. Dendievel, and H. Sallée, "Realization, test and modelling of honeycomb wallboards containing a phase change material," *Energy and Buildings*, vol. 43, no. 1, pp. 232–238, 2011.

[25] B. Xie, W.-l. Cheng, and X. Zhi-ming, "Studies on the effect of shape-stabilized PCM filled aluminum honeycomb composite

material on thermal control," *International Journal of Heat and Mass Transfer*, vol. 91, pp. 135–143, 2015.

[26] M. Abuşka, S. Şevik, and A. Kayapunar, "Experimental analysis of solar air collector with PCM-honeycomb combination under the natural convection," *Solar Energy Materials & Solar Cells*, vol. 195, pp. 299–308, 2019.

[27] M. Pagliaro and F. Meneguzzo, "Lithium battery reusing and recycling: a circular economy insight," *Heliyon*, vol. 5, p. 01866, 2019.

[28] J. Zhang, X. Li, G. Zhang et al., "Characterization and experimental investigation of aluminum nitride-based composite phase change materials for battery thermal management," *Energy Conversion and Management*, vol. 204, p. 112319, 2020.

[29] C. Kai, C. Yiming, S. Yiqi, S. Mengxuan, W. Shuangfeng, and C. Lin, "Construction of effective symmetrical air-cooled system for battery thermal management," *Applied Thermal Engineering*, vol. 166, p. 114679, 2020.

[30] Y. Li, J. Yang, and J. Song, "Design principles and energy system scale analysis technologies of new lithium-ion and aluminum-ion batteries for sustainable energy electric vehicles," *Renewable and Sustainable Energy Reviews*, vol. 71, pp. 645–651, 2017.

[31] G. N. Tiwari, R. K. Mishra, and S. C. Solanki, "Photovoltaic modules and their applications: a review on thermal modelling," *Applied Energy*, vol. 88, no. 7, pp. 2287–2304, 2011.